JGR Oceans

RESEARCH ARTICLE
10.1029/2018JC014480

Variations of Equatorial Shear, Stratification, and Turbulence Within a Tropical Instability Wave Cycle

Ryuichiro Inoue[1], Ren-Chieh Lien[2], James N. Moum[3], Renellys C. Perez[4], and Michael C. Gregg[2]

[1]Research and Development Center for Global Change, Japan Agency for Marine-Earth Science and Technology, Yokosuka, Japan, [2]Applied Physics Laboratory, University of Washington, Seattle, WA, USA, [3]College of Earth, Ocean and Atmospheric Sciences, Oregon State University, Corvallis, OR, USA, [4]Atlantic Oceanographic and Meteorological Laboratory, National Oceanic and Atmospheric Administration, Miami, FL, USA

Key Points:
- Moored observations capture variations of shear, stratification, and turbulence during equatorial Pacific tropical instability waves (TIWs)
- Shear and stratification within the deep-cycle layer were modulated by the phase of each TIW, whereas turbulence exhibited less modulation
- An ocean model forced with observed winds gave dynamical insight on the dependence of shear and stratification on the phase of the TIW cycle

Correspondence to:
R. Inoue,
rinoue@jamstec.go.jp

Citation:
Inoue, R., Lien, R.-C., Moum, J. N., Perez, R. C., & Gregg, M. C. (2019). Variations of equatorial shear, stratification, and turbulence within a tropical instability wave cycle. *Journal of Geophysical Research: Oceans*, *124*, 1858–1875. https://doi.org/10.1029/2018JC014480

Received 16 AUG 2018
Accepted 18 FEB 2019
Accepted article online 20 FEB 2019
Published online 21 MAR 2019

Abstract Equatorial Internal Wave Experiment observations at 0°, 140°W from October 2008 to February 2009 captured modulations of shear, stratification, and turbulence above the Equatorial Undercurrent by a series of tropical instability waves (TIWs). Analyzing these observations in terms of a four-phase TIW cycle, we found that shear and stratification within the deep-cycle layer being weakest in the middle of the N-S phase (transition from northward to southward flow) and strongest in the late S phase (southward flow) and the early S-N phase (transition from southward to northward flow). Turbulence was modulated but showed less dependence on the TIW cycle. The vertical diffusivity (K_T) was largest during the N (northward flow) and N-S phases, when stratification was weak, despite weak shear, and was smallest from the late S phase to the S-N phase, when stratification was strong, despite strong shear. This tendency was less clear in turbulent heat flux because vertical temperature gradients were small at times when K_T was large, and large when K_T was small. We investigated the dynamics of shear and stratification variations within the TIW cycle by using an ocean general circulation model forced with observed winds. The model successfully reproduced the observed strong shear and stratification in the S phase, except for a small phase difference. The strong shear is explained by vortex stretching by TIWs. The strong stratification is explained by meridional and vertical advection.

Plain Language Summary Moored observations in the central equatorial Pacific during 2008 La Niña captured a series of tropical instability waves (TIWs). Vertical shear of horizontal velocity, stratification, and turbulent mixing above the Equatorial Undercurrent varied strongly in different phases of each TIW cycle. The dynamics of modulations of stratification and shear by the TIW cycle were identified using results from an oceanic model.

1. Introduction

Tropical instability waves (TIWs), also called tropical instability vortices (Kennan & Flament, 2000), are prominent features in the central and eastern equatorial Pacific during boreal fall and winter (e.g., Lyman et al., 2005, 2007) and in the central and eastern Atlantic during boreal summer and fall (e.g., Grodsky et al., 2005; Perez et al., 2012). Past studies have shown the importance of TIWs to the ocean's surface mixed layer heat budget (e.g., Jochum et al., 2007; Jochum & Murtugudde, 2006; Menkes et al., 2006), salinity (e.g., Lee et al., 2012), biogeochemical properties (e.g., Evans et al., 2009), and equatorial dynamics (e.g., Grodsky et al., 2005; Holmes et al., 2014; Holmes & Thomas, 2015; Masina et al., 1999; Philander, 1978; Qiao & Weisberg, 1998; Z. Yu et al., 1995). Strong convergent and divergent flows associated with TIWs may influence vertical shear and stratification, which ultimately modulate turbulence on diurnal to seasonal time scales (Chereskin et al., 1986; Dutrieux et al., 2008; Halpern et al., 1988; Holmes et al., 2014; Holmes & Thomas, 2015; Hormann et al., 2013; Johnson et al., 2002; Kennan & Flament, 2000; Masina & Philander, 1999; Moum et al., 2013; Perez et al., 2010; Toole et al., 1987; Wenegrat & McPhaden, 2015). Observations have documented variations of shear, stratification, and turbulence in different parts of a single TIW cycle in the equatorial Pacific, while this study is the first analysis of multiple TIW cycles.

Several major observational campaigns concerned with ocean turbulence have been conducted in the central equatorial Pacific at 0°, 140°W, including Tropic Heat 1 in 1984 (Gregg et al., 1985; Moum et al., 1989;

Moum & Caldwell, 1985), Tropic Heat 2 in 1987 (Peters et al., 1991), and the Tropical Instability Wave Experiment in 1991 (Lien et al., 1995; Moum et al., 1995). These experiments revealed the unique nature of deep-cycle turbulence and its absence during El Niño events, the warm phase of the El Niño-Southern Oscillation (ENSO). Deep-cycle turbulence is a strong nighttime turbulence, more than 10 times the magnitude of daytime turbulence and comparable to the turbulence in the surface mixed layer, that penetrates into a stratified shear layer tens of meters below the base of the surface mixed layer (e.g., Pham et al., 2013; Smyth & Moum, 2013). Deep-cycle turbulence is a significant part of the heat budget of the surface mixed layer in the central equatorial Pacific (e.g., Moum et al., 2013).

Previous measurements taken during TIW events in the central equatorial Pacific using Lagrangian floats, microstructure profilers, and moorings have revealed that TIW events strongly modulate the depth, stratification, and vertical shear of the surface mixed layer as well as deep-cycle turbulence (Inoue et al., 2012; Lien et al., 2002, 2008; Moum et al., 2009). Inoue et al. (2012) discussed this modulation during four different phases of one TIW at 0°, 140°W observed during the Equatorial Internal Wave Experiment (EQUIX). They divided the TIW cycle into four phases according to the phase of the meridional velocity: northward flow (N phase), the transition from northward to southward flow (N-S phase), southward flow (S phase), and the transition from southward to northward flow (S-N phase). The N-S phase was shown to have the largest values of reduced shear squared (shear squared minus four times stratification squared), the thickest nighttime surface mixed layer, the deepest penetration of deep-cycle turbulence, the largest turbulent heat flux, and the largest integrated turbulence kinetic energy dissipation rate in the deep-cycle layer. The S phase featured the thinnest nighttime surface mixed layer and the shallowest penetration of deep-cycle turbulence.

In this paper, we extend Inoue et al.'s (2012) analysis by investigating the effects of a sequence of six TIWs on the upper equatorial shear, stratification, and turbulence on the basis of observations at the 0°, 140°W EQUIX mooring. In section 2, we examine the TIW characteristics using satellite sea surface temperature (SST) observations and vertically averaged properties observed at the EQUIX mooring. The EQUIX data are presented, and a composite view of the variations of velocity, shear, stratification, and turbulent parameters in the upper equatorial ocean in different phases of the TIW cycle is constructed from these data in section 3. Turbulent thermal diffusivity and turbulent heat flux are computed using measurements taken by the thermal variance sensor χpods (Moum & Nash, 2009; Perlin & Moum, 2012). In section 4, an ocean general circulation model (OGCM) is used to identify the three-dimensional processes responsible for the variations of background shear and stratification in different phases of the TIW cycle. Section 5 discusses the modulation of deep-cycle turbulence in different phases of the TIW cycle. Results are summarized in section 6.

2. Moored and Satellite Observations of a Train of Six TIWs

2.1. Experiment

The EQUIX mooring was deployed over two periods: the *intensive observational period* from 23 October to 8 November 2008 and the *extensive observational period* from 11 November 2008 to 3 March 2009 (Inoue et al., 2012).

During the intensive observational period, the mooring was equipped with 20 Seabird SBE37 recorders equipped with pumped conductivity-temperature-pressure (CTD) sensors, 10 moored thermal variance sensor χpods, and 3 acoustic Doppler current profilers (ADCPs) in the upper 100 m. During the extensive observational period, the mooring was equipped with 20 Seabird SBE37 recorders with pumped CTD sensors, 8 χpods, and 2 ADCPs in the upper 100 m. Depths and sampling rates of sensors are summarized in Table 1.

The methods we used to estimate the thermal variance dissipation rate, χ_T; the turbulent thermal diffusivity, K_T; and the turbulent temperature flux, H_F, using χpod measurements have been described in detail in Moum and Nash (2009) and are only briefly summarized here. The thermal variance dissipation rate, χ_T, is computed using microstructure temperature measurements taken by χpods (Table 1). The turbulent thermal diffusivity is computed as $K_T = \frac{\chi_T}{2\left(\overline{T}_z\right)^2}$, where $\overline{T}_z$ is the vertical gradient of the background temperature, computed from the cable motion following Moum and Nash (2009). $\overline{T}_z$ was computed this way because temperature measurements taken from 11 CTD sensors positioned about 1 m apart in the nominal depth

Table 1
Sampling Rates, Deployment Depths, and Configurations of Sensors Used in This Study on the EQUIX Mooring

		Depth (m)	
Type	Sampling rate	IOP	EOP
SeaBird CTD: SBE37	7 s (IOP) 60 s (EOP)	1, 25.5, 26.5, 27.5, 29.5, 30.5, 31.5, 33.5, 34.5, 35.5, 36.5, 37.5, 38.5, 44.3, 45.3, 46.3, 47.3, 49.3, 50.3, 52.3	25.5, 26.5, 27.5, 29.5, 30.5, 31.5, 33.5, 34.5, 35.5, 36.5, 37.5, 38.5, 44.3, 45.3, 46.3, 47.3, 49.3, 50.3, 52.3, 53.3
χpod[a]	T, 10 Hz dT/dt, 120 Hz P, 10 Hz Three-axis accelerations, 120 Hz Compass, 1 Hz	24.5, 28.5, **32.5**, 48.3, 51.3, 53.3, 62.3, **71.3**, 80, **91**	**24.5**, 28.5, 32.5, **48.3**, 51.3, 54.3, 62.3, 80
Upward looking 300-kHz ADCP[b]	2 Hz	90	

Note. ADCP, acoustic Doppler current profiler; CTD, conductivity-temperature-pressure; EQUIX, Equatorial Internal Wave Experiment; IOP, intensive observational period; EOP, extensive observational period.
[a]χpod depths in boldface represent sensors that failed during the deployment period. [b]Bin size, 2 m; penetration range, 90 m; pulse size, 2 m.

range 25.5–38.5 m, and 8 sensors positioned similarly in the depth range 44.3–53.3 m were shallower than the deepest χpod's depth (Table 1). One-hour averages of χ_T and $\overline{T}_z$ are used to calculate subsurface turbulent temperature flux H_F using the formula $H_F = -\rho C_p K_T \overline{T}_z = -\rho C_p \chi_T / 2\overline{T}_z$. Potential density, ρ, was calculated using the vertically averaged potential density from moored CTDs. H_F values below the mixed layer are generally negative at the EQUIX mooring site.

EQUIX mooring data were collected during the final stage of the 2008–2009 La Niña (Moum et al., 2013). The TIWs observed at this time were stronger than those observed during ENSO neutral years (Moum et al., 2013), consistent with previous studies (Baturin & Niiler, 1997; Contreras, 2002; Wu & Bowman, 2007). Daily average surface heat flux and wind measured on a NOAA Tropical Atmosphere Ocean (TAO) buoy ~9 km south of the EQUIX mooring site were used in this analysis (see Figure 1 of Perlin & Moum, 2012).

2.2. TIW Surface Signatures

Daily SST fields from the Tropical Rainfall Measuring Mission Microwave Imager, with a 3-day running mean at 0.25° × 0.25° spatial resolution, revealed the surface signature of a series of seven TIWs passing the EQUIX mooring during the study period (Figure 1). Because the CTD sensors ran out of power and the data were incomplete for the seventh TIW, we discuss only the first six TIWs in the following analysis. We define the TIW period as the time interval between consecutive maxima in northward velocities, after low-pass filtering at 0.1 cpd and vertically averaging over 10- to 80-m depth (Figure 2a). The six TIWs had periods ranging from 15 to 24 days, with the sixth TIW being the longest and the second and fourth TIWs being the shortest. At the tail end of the third TIW, near mid-December, the meridional current averaged over 10- to 80-m depth nearly vanished because the current was northward in the upper 40 m and southward in the lower 40 m (Figure 3c). During the passage of the third and fourth TIWs, the typical cusped SST patterns associated with TIWs (weaker SST perturbations and horizontal temperature gradients) did not appear in the satellite SST data (Figures 1c and 1d). This may be a result of interactions between the third and fourth TIWs or modulation by other equatorial processes. Altimetric sea level anomalies (not shown) show evidence of a downwelling (positive sea level anomaly) immediately followed by an upwelling (negative anomaly) equatorial Kelvin wave that propagate from the west and reach the EQUIX mooring just prior to the first and third TIW, respectively. Modeling results by Holmes and Thomas (2016) find that TIW eddy kinetic energy will damp (grow) following the passage of a downwelling (upwelling) equatorial Kelvin wave, with largest response a month to 2 months after the wave passes. This timing is consistent with the presence of weak third and fourth TIWs approximately a month after the downwelling wave passes and strong fifth and six TIWs approximately a month after the upwelling wave passes.

Surface heat flux varied at time scales comparable to the TIW period (Figure 2b), with positive heat flux anomalies during the N phase and negative anomalies during the S phase. The surface wind stress showed notable variations on TIW time scales as well as shorter time scales (Figure 2c), with the strongest positive wind stress anomalies typically occurring during the S phase. The variations of surface heat flux and surface

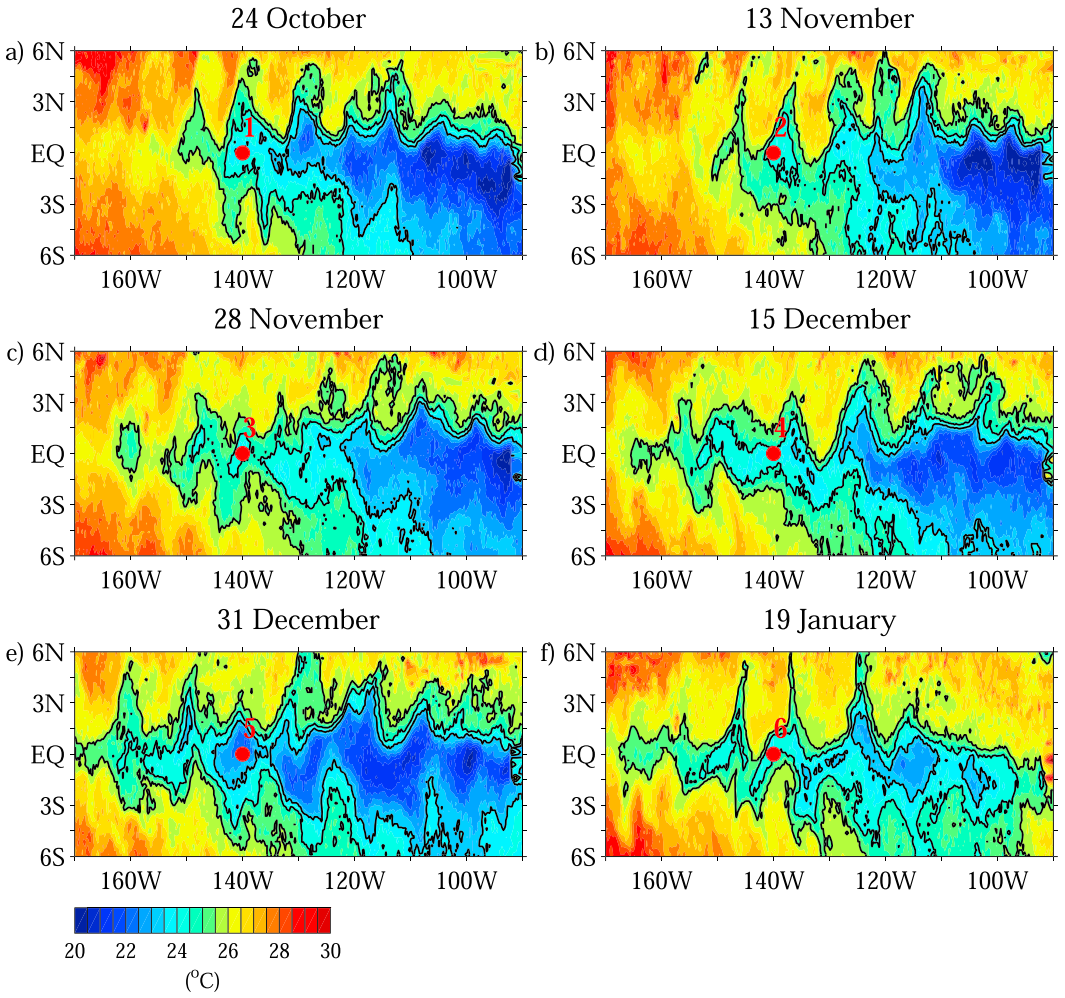

Figure 1. Sea surface temperature (SST) from satellite observations on (a) 24 October 2008, (b) 13 November 2008, (c) 28 November 2008, (d) 15 December 2008, (e) 31 December 2008, and (f) 19 January 2009. These dates correspond to the starting times of the six tropical instability waves (TIWs) observed at the mooring location (red dots) as determined by the maximum in northward flow.

wind stress on TIW time scales were consistent with the modulation of air-sea fluxes by TIWs demonstrated by previous studies (e.g., Seo et al., 2007).

Vertically averaged subsurface salinity showed positive anomalies in the N-S flow transition and negative anomalies in the S-N flow transition (Figure 2e). These variations can be explained by the northward advection of salty equatorial cold-tongue water across the EQUIX mooring during the N-S phase and southward advection of fresher water during the S-N phase, as simulated in an OGCM model to be discussed later. The satellite salinity observations (e.g., Lee et al., 2012) also reasonably captured the temporal variation of salinity associated with TIWs. SST and vertically averaged subsurface temperature also showed variations at periods near that of the TIWs and at longer timescales associated with other processes modulating the temperature budget, such as surface heating (Figure 2b). Vertically averaged subsurface potential density (Figure 2f) was controlled mostly by subsurface temperature (Figure 2d). Details of vertical structures of the upper central equatorial ocean observed at the EQUIX mooring site are examined in the next section.

3. Upper Equatorial Shear, Stratification, and Turbulence

The zonal velocity data depict the typical westward flowing South Equatorial Current in the upper layer overlying the eastward flowing Equatorial Undercurrent, with strong modulation by the TIWs such that the strongest westward flow near the surface was typically around the S phase (Figure 3b). The

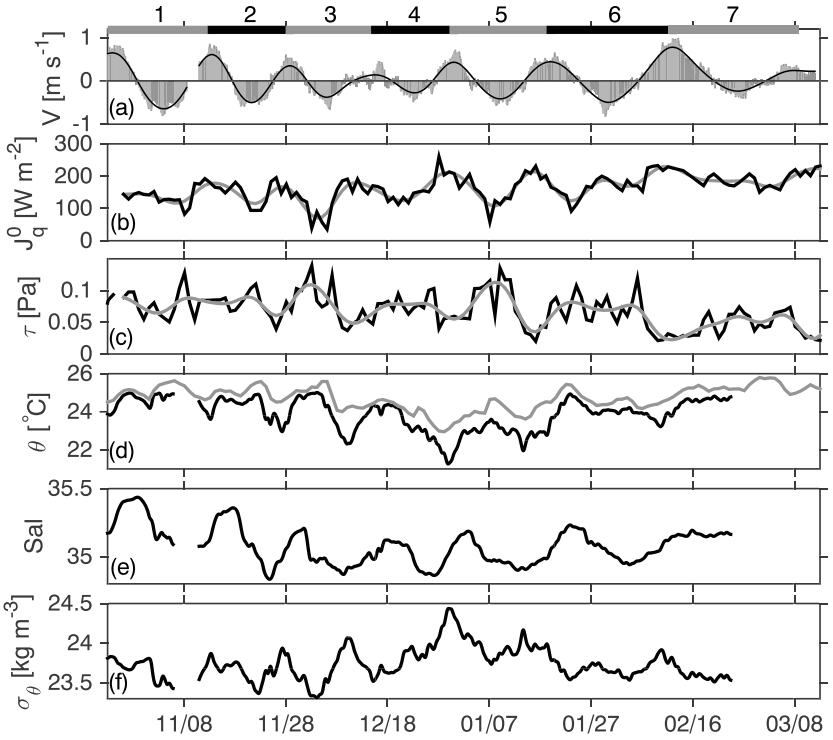

Figure 2. Observations of the Equatorial Internal Wave Experiment (EQUIX) mooring during the study period. Tropical instability wave (TIW) periods 1 through 7 are labeled at the top. Time ticks are 20 days apart. (a) Hourly average meridional velocities averaged over the depth interval 10–80 m (gray bars) and low-pass filtered velocities at 0.1 cpd (black). (b) Surface heat flux (daily net heating); daily averages are in black, and low-pass filtered flux is in gray. (c) Daily average wind stress magnitude (black) and low-pass filtered data at 0.1 cpd (gray). (d) Potential temperature averaged over the depth interval 30–50 m (black), approximating the deep-cycle layer, and sea surface temperature (SST; gray). (e) Salinity averaged over the depth interval 30–50 m. (f) Potential density averaged over the depth interval 30–50 m. Mooring data in (d)–(f) are low-pass filtered at 1 cpd for presentation purposes.

meridional velocity perturbations associated with TIWs mostly penetrated down to 80-m depth, except during the transition from the third to fourth TIW (Figure 3c). The observed vertical shear squared of the zonal current U, $(\partial_z U)^2$, was typically stronger than the shear squared of the meridional current V, $(\partial_z V)^2$, and dominated the total shear squared, $Sh^2 = (\partial_z U)^2 + (\partial_z V)^2$ (Figures 3d–3f). The depth of the maximum in Sh^2 varied between 40 and 80 m, and the shallowest maximum in meridional shear squared often occurred during the S-N phase, when the penetration depth of the meridional current was shallowest (Figures 3c and 3e). During the fourth TIW, the meridional shear squared was weak (Figure 3e), but the total shear squared remained large near 70-m depth during all phases of this TIW (Figure 3f). Turbulence was measured by χpods at only six depths. Thermal dissipation was strong mostly at depths shallower than the depth of maximum shear (above the black curve in Figure 3g) and weak below the depth of maximum shear, consistent with previous observations of deep-cycle turbulence (e.g., Lien et al., 1995; Moum et al., 2009).

We derived fields for meridional current velocity V, total shear squared Sh^2, buoyancy frequency squared N^2, turbulent thermal diffusivity K_T, and turbulent temperature flux H_F within a composite TIW cycle made by combining the six TIWs (Figure 4). The time within each TIW cycle was expressed as a nondimensional time (NDT) that renders the TIW cycle in terms of $T/2\pi$ (where T is the period of the corresponding TIW) such that NDT = 0 represents the time of maximum vertically averaged northward flow, the beginning of a TIW, and NDT = π represents the time of maximum southward flow, the midpoint of a TIW. The four TIW phases were defined as follows: N phase = $(0 \pm 0.125) \times 2\pi$, N-S phase = $(0.25 \pm 0.125) \times 2\pi$, S phase = $(0.5 \pm 0.125) \times 2\pi$, and S-N phase = $(0.75 \pm 0.125) \times 2\pi$ (Figure 2a). Measurements were averaged vertically over the layer defined by the shallowest available measurements (see Table 1) and the depth of maximum shear (black curve in Figure 3f), which served as a proxy for the penetration depth of deep-

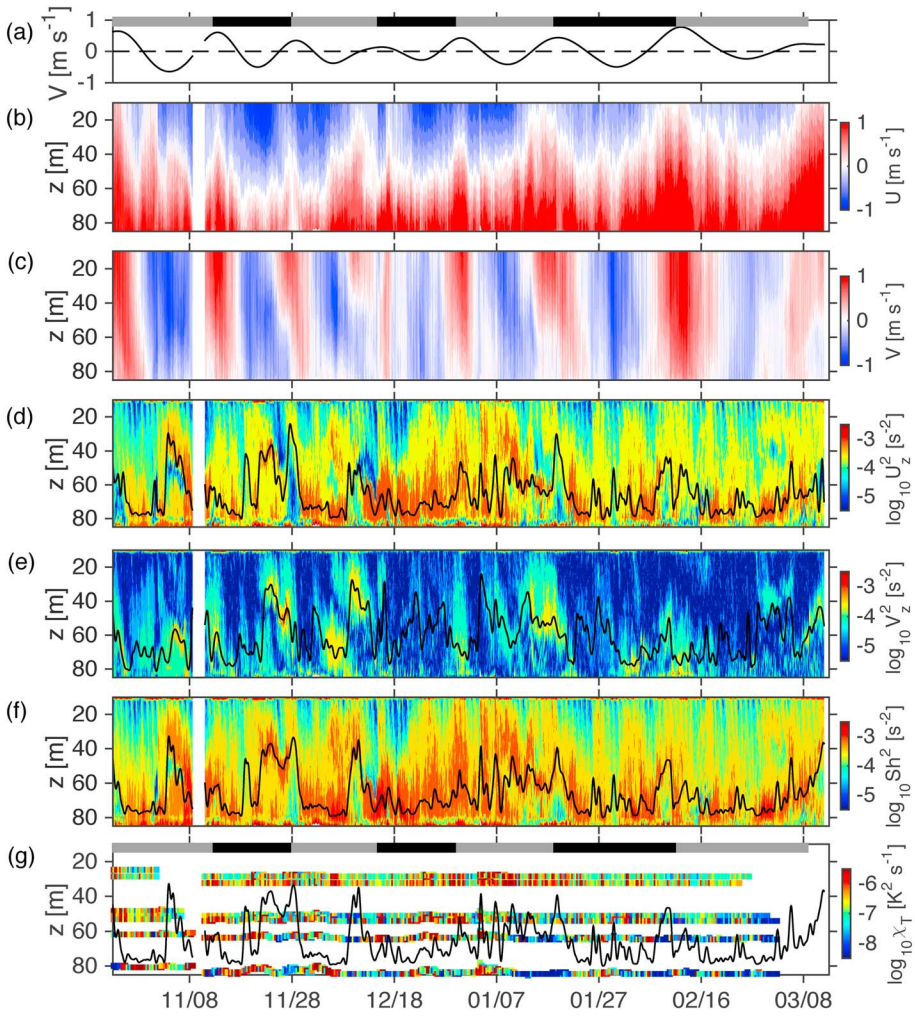

Figure 3. Mooring observations at 0°, 140°W with seven tropical instability wave (TIW) periods shown at top and bottom. (a) Meridional velocity averaged over the depth interval 10–80 m, low-pass filtered at 0.1 cpd. Depth-time contour plots of hourly average observations of (b) zonal velocity U (colors) and temperature (black, contour interval 1 °C), (c) meridional velocity V, (d) square of the vertical shear of U, (e) square of the vertical shear of V, (f) total shear squared, and (g) thermal dissipation rate, χ_T, observed at the mooring. The black lines in (d) and (e) mark the maximum shear squared layer for each velocity component. The black lines in (f) and (g) mark the layer of maximum total shear squared, assumed to be the base of the deep-cycle layer.

cycle turbulence. Note that although the vertical average of V started at 10-m depth, Sh^2 was averaged from 25 m for comparison with N^2. All fields were then temporally averaged over the six TIWs as a function of NDT to yield variations in a composite TIW cycle.

Within this composite TIW, vertically averaged Sh^2 and N^2 exhibit a similar temporal variation (Figures 4b and 4c). Sh^2 and N^2 are the strongest during NDT = 1–1.5 π, in the S phase and the early S-N phase and are weak around NDT = 0.5 π, in the N-S phase, and 1.75 π, the late S-N phase. Processes responsible for these variations are discussed in section 4. Note that although the composite indicates that the EQUIX mooring observed the same pattern as the EQUIX shipboard measurements documented in Inoue et al. (2012), it is possible that some of the variability of Sh^2 could be missed because the moored ADCP only measured the upper 80 m of the water column. It is also possible that N^2 is underestimated by the vertical averaging when the depth of maximum vertical shear is deep because our CTD sensors are shallower than the top of the Equatorial Undercurrent where the stratification is strong (Table 1).

The vertically averaged composites of K_T are larger in the N and N-S phases than in the S and S-N phases (Figure 3d). However, the TIW phase dependence is not as pronounced as it is for shear and stratification.

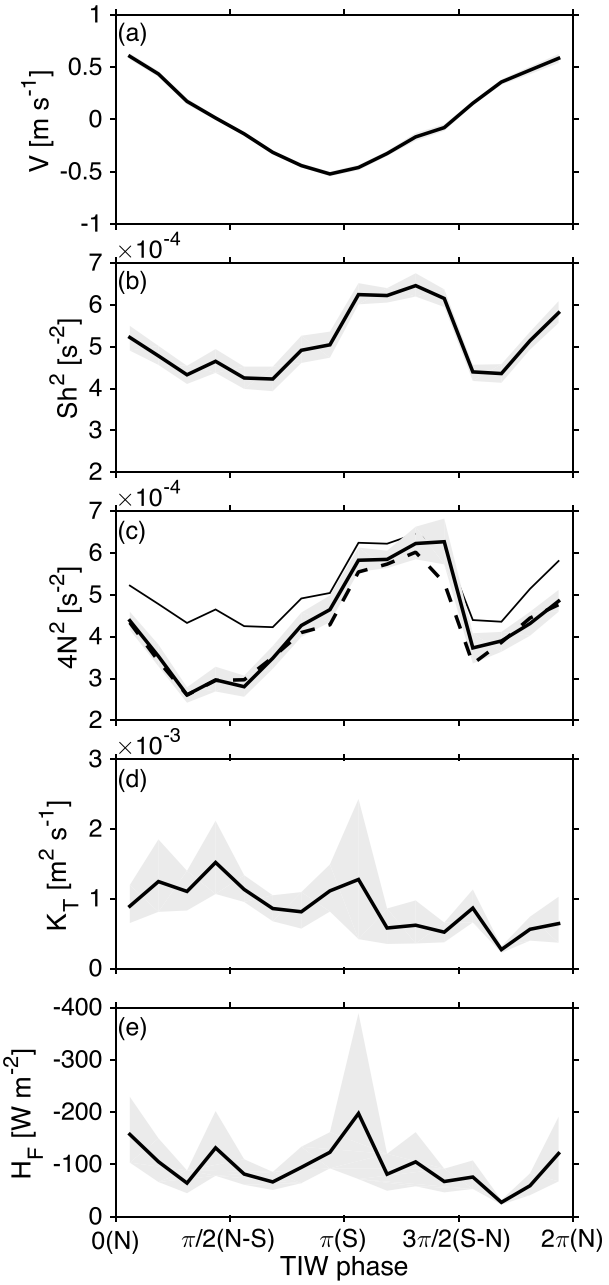

Figure 4. Composite plots for the six observed tropical instability waves (TIWs) as a function of nondimensional time (NDT), showing arithmetic means of vertically averaged (a) meridional velocity, (b) shear squared, (c) buoyancy frequency squared times 4, (d) vertical diffusivity of heat, and (e) heat flux. The gray shading shows the 95% confidence interval from the bootstrap method (Efron & Gong, 1983). The thin and thick dashed lines in (c) are the average shear squared shown in (b) and the shear squared averaged over the same depth range as buoyancy frequency squared, respectively.

This may reflect imprecision arising from the small number of measurements (6) in the deep-cycle layer or the strong intrinsic variability of turbulence compared to shear and stratification, as implied by their respective confidence intervals (gray shading in Figure 4). Variations of turbulent heat flux over the TIW cycle are not as clear as the K_T variations because of the large K_T(Figure 4d) and small temperature gradient $\overline{T_z}$ (not shown) in the first half of the TIW and the small K_T and large $\overline{T_z}$ in the second half. Details of the variations of K_T and H_F over the TIW cycle are discussed further in section 5.

4. Model Simulations of TIWs: Effects on Shear and Stratification

4.1. Illustration of Meridional Advection Effect on Sh^2 and N^2 in the OGCM

To investigate the processes responsible for the observed temporal variations of Sh^2 and N^2 within the TIW cycle, we used an OGCM, which is same as in Perez and Kessler (2009) and Perez et al. (2010), to study the three-dimensional structure and evolution of TIWs. Daily averages of model results from a regional Modular Ocean Model (MOM4; Griffies et al., 2003) simulation in the tropical Pacific were used to reveal prominent features of TIWs between September 1999 and October 2009 (following Perez et al., 2010). The model, forced with monthly Quick Scatterometer (QuikSCAT) wind stress, has a meridional resolution of 0.33° and zonal resolution of 0.625° near the equator and includes 49 vertical levels of 10-m resolution in the upper 220 m. Constant along-stream and cross-stream horizontal viscosities (2,000 and 1000 m^2/s, respectively) and KPP parameterization (Large et al., 1994) for vertical mixing are used (see Appendix A for additional details). Although the modeled TIWs are of smaller magnitude than the observed TIWs, the OGCM simulations generated the equatorial current system (e.g., South Equatorial Current, Equatorial Undercurrent, North Equatorial Counter Current, and meridional-vertical tropical cells) and thermocline as well as TIWs with realistic three-dimensional structures and temporal evolution (Perez et al., 2010; Perez & Kessler, 2009).

Cross-equatorial vertical sections along 140°W of the model TIW during the N-S and S phases illustrate the effect of meridional advection on the upper equatorial Sh^2 and N^2 (Figure 5). The simulated Sh^2 and N^2 at 0°, 140°W at depths of 20–70 m are weaker during the N-S phase (Figures 5c and 5e) than during the S phase (Figures 5d and 5f). In the middle of the N-S phase, when the TIW meridional current begins to change sign from northward to southward, the surface expression of the cold-tongue front (defined using maximum meridional SST gradients following Perez et al., 2010) is at its farthest north of the equator (red triangle in Figure 5a). The divergent zone of the TIW's meridional velocity ($\partial_y V > 0$) is around 2°N (Figure 5g). As the TIW current turns southward, the cold-tongue front shifts nearly 350 km southward from 4.15 to 0.85°N because the highest horizontal temperature gradient exists at the southern edge of the TIW (Figure 5b) and the strong divergent zone is at the front (Figure 5h). The southward shift of the cold-tongue front decreases with depth because the TIW meridional current decreases with depth. Consequently, the cold-tongue front slopes northward with increasing depth (contours in Figure 5f) and leads to larger N^2 above 70 m during the S phase both at and north of the equator (colors in Figure 5f). The southward advection leads to

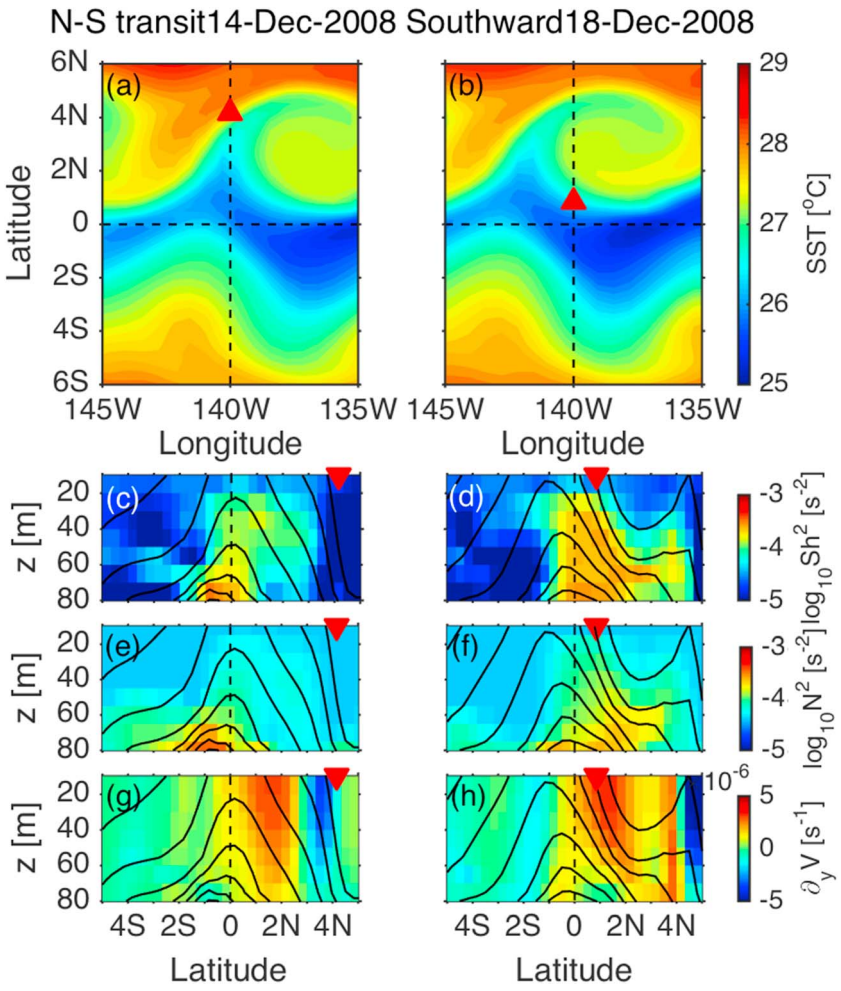

Figure 5. Ocean general circulation model (OGCM) simulation of sea surface temperatures (SSTs) on (a) 14 December (transition between northward and southward flow) and (b) 18 December 2008 (southward flow). The red triangle indicates the position of a front along 140°W. The lower plots show cross-equatorial vertical sections of simulated Sh^2, N^2, and $\partial_y V$ on (c, e, and g) 14 December and (d, f, and h) 18 December 2008. Contours indicate density.

elevated Sh^2 at 0°, 140°W in the model during the S phase (Figure 5d). These model results illustrate how meridional advection could play a role in the evolution of Sh^2 and N^2 associated with a TIW at 0°, 140°W when examined in the Eulerian framework. The next section examines the contributions of TIW meridional, as well as zonal, advection effects and other processes in the formulation of tendency terms for shear and stratification in the Eulerian framework.

4.2. Estimating Tendency Terms for Shear and Stratification

Following the analysis of observations to form a composite TIW discussed in section 3.1, Figures 6 and 7 presents the average model fields of seven simulated TIWs as a function of NDT that are also vertically averaged over depths of 10–60 m. The vertically averaged Sh^2 and N^2 exhibit notable temporal variations over the TIW cycle (Figures 6a and 7a). Shear and stratification increase during the S phase and reach their maximum values at the end of the S phase, which is qualitatively similar to the observed TIWs, but with a slight phase difference between the peaks in Sh^2 and N^2 (compare Figures 6a and 7a with Figures 4b and 4c).

As was the case with the observations (Figure 3), the simulated vertical shear is dominated by the zonal current component (not shown). The time evolution of the vertical shear of the zonal current, $Sh_x = \partial_z U$, at the EQUIX mooring site can be expressed as

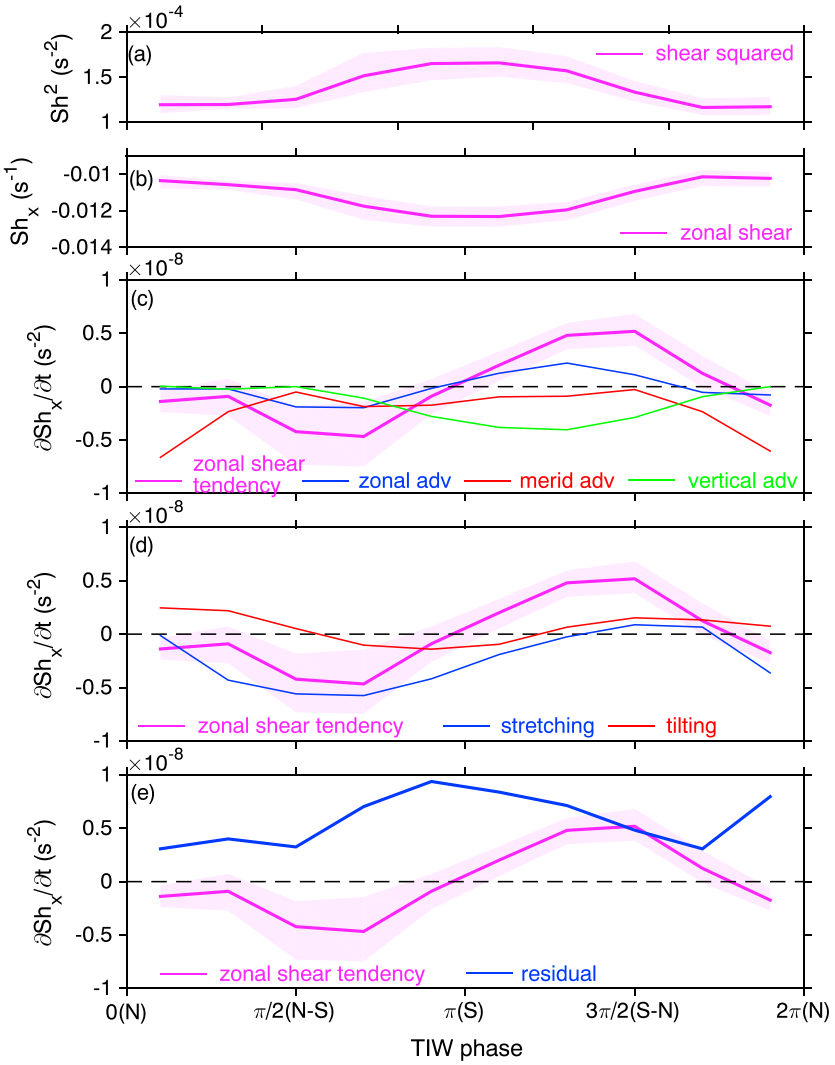

Figure 6. Plots of vertically averaged (a) shear squared, (b) zonal shear, and (c–e) tendency of zonal shear for a composite of seven model TIWs between 13 October 2008 and 3 March 2009. The magenta curves with shading represent the mean and 95% confidence intervals estimated by the bootstrap method (Efron & Gong, 1983), respectively. The blue line, red line, and green line in (c) represent contributions from zonal, meridional, and vertical advection, respectively. The blue and red lines in (d) represent contributions from the horizontal vortex stretching and tilting terms, respectively. The thick blue line in (e) is the residual term, which approximates the averaged vertical gradient of pressure and friction terms and also includes errors.

$$\frac{\partial Sh_x}{\partial t} = -\frac{\partial}{\partial z}\left(U\frac{\partial U}{\partial x}\right) - \frac{\partial}{\partial z}\left(V\frac{\partial U}{\partial y}\right) - \frac{\partial}{\partial z}\left(W\frac{\partial U}{\partial z}\right) + \frac{\partial}{\partial z}(\text{pressure} + \text{friction}), \tag{1}$$

where U, V, and W are three-dimensional velocity components from the model and *pressure* and *friction* represent the pressure gradient force and friction (it represents wind forcing at the sea surface), respectively (Appendix A). The Coriolis term is negligible at the equator. Using the continuity equation ($\partial_z W = -\partial_x U - \partial_y V$), (1) can be rewritten as

$$\frac{\partial Sh_x}{\partial t} = -U\frac{\partial Sh_x}{\partial x} - V\frac{\partial Sh_x}{\partial y} + Sh_x\frac{\partial V}{\partial y} - \frac{\partial V}{\partial z}\frac{\partial U}{\partial y} - W\frac{\partial Sh_x}{\partial z} + \frac{\partial}{\partial z}(\text{pressure} + \text{friction}). \tag{2}$$

The first two terms on the right-hand side of (2) represent horizontal advection; the third and fourth terms represent vortex stretching and tilting, respectively; and the fifth term represents vertical

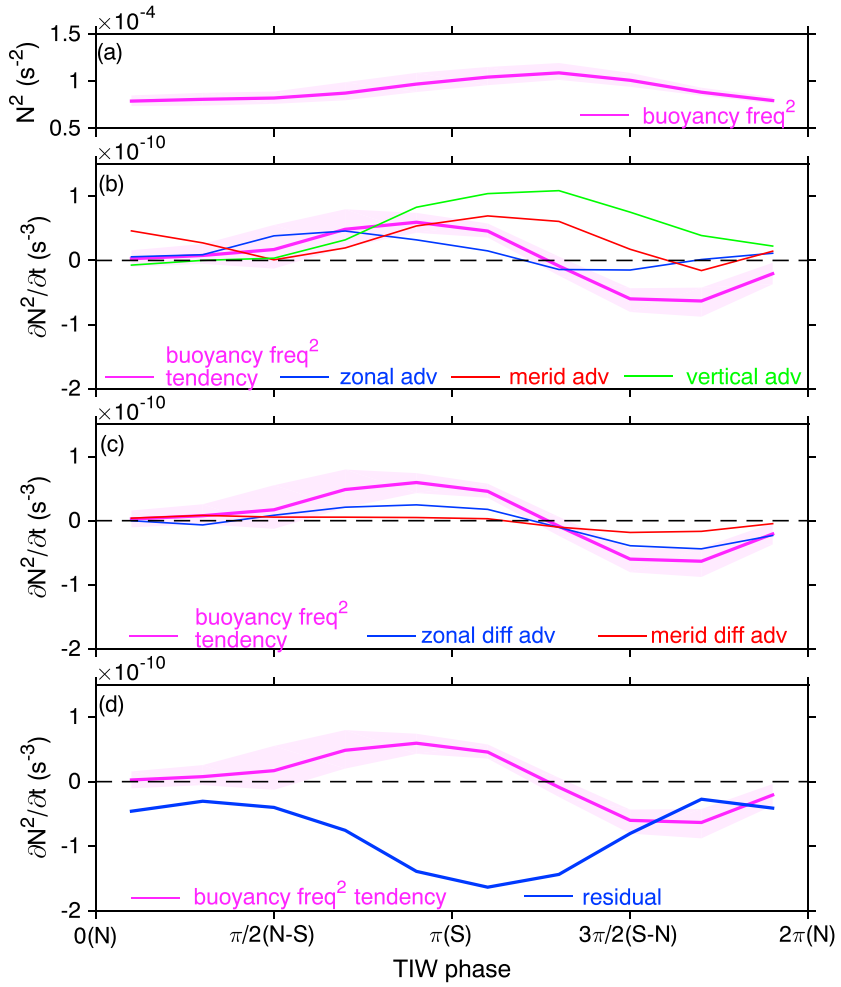

Figure 7. Composite plots of vertically averaged (a) buoyancy frequency squared and (b–d) tendency of buoyancy frequency squared as shown in Figure 6. The magenta curves with shading represent the mean and 95% confidence intervals estimated by the bootstrap method (Efron & Gong, 1983), respectively. The thin blue line, red line, and green line in (b) represent contributions from zonal, meridional, and vertical advection, respectively. The blue and red lines in (c) represent contributions from the first and second of differential advection of buoyancy terms, respectively. The thick blue line in (d) is the residual term, which approximates the averaged vertical gradient of diffusion and forcing terms and also includes errors.

advection. We note that although the Eulerian framework is useful to describe variabilities observed in the EQUIX mooring, advection itself does not generate vertical shear. The ultimate source of this vertical shear arises from the other terms in (2), which are more clearly exposed using a Lagrangian analysis (e.g., Holmes & Thomas, 2015).

The evolution of stratification at the EQUIX mooring site can be similarly written as

$$\begin{aligned}\frac{\partial N^2}{\partial t} &= \frac{g}{\rho}\frac{\partial}{\partial z}\left(U\frac{\partial \rho}{\partial x}\right)+\frac{g}{\rho}\frac{\partial}{\partial z}\left(V\frac{\partial \rho}{\partial y}\right)+\frac{g}{\rho}\frac{\partial}{\partial z}\left(W\frac{\partial \rho}{\partial z}\right)-\frac{g}{\rho}\frac{\partial}{\partial z}(\text{diffusion}+\text{forcing})\\ &= -U\frac{\partial N^2}{\partial x}-V\frac{\partial N^2}{\partial y}+\frac{g}{\rho}Sh_x\frac{\partial \rho}{\partial x}+\frac{g}{\rho}\frac{\partial V}{\partial z}\frac{\partial \rho}{\partial y}+\frac{g}{\rho}\frac{\partial}{\partial z}\left(W\frac{\partial \rho}{\partial z}\right)-\frac{g}{\rho}\frac{\partial}{\partial z}(\text{diffusion}+\text{forcing}).\end{aligned} \tag{3}$$

Here $N^2=-\frac{g}{\rho}\frac{\partial \rho}{\partial z}$. A minus sign in the right-hand side of (3) is due to the definition of N^2. The first two terms on the right-hand side of (3) are horizontal advection terms, the third and fourth terms represent differential

advection of buoyancy, the fifth term represents the vertical gradient of vertical advection of density, and *diffusion* and *forcing* represent diffusion and buoyancy forcing, respectively (see Appendix A).

With the daily-averaged model fields that were available from the OGCM simulation, we were limited to examining the zonal shear tendency, horizontal and vertical advection, and horizontal stretching term in (2) and the stratification tendency, horizontal and vertical advection, and differential advection of buoyancy terms in (3). Sh^2, N^2, and these terms were averaged over series of seven model TIWs as a function of NDT and averaged vertically over the depth interval 10–60 m (Figure 6).

4.3. Evolution of Shear and Stratification in the Composite Model TIW

The westward flowing South Equatorial Current atop the eastward flowing Equatorial Undercurrent imposes a background negative zonal shear Sh_x in the upper equatorial ocean. The zonal shear tendency term is negative during NDT = 0 to π as the TIW progresses from the N to the S phase (Figures 6c–6e), and it means the increase in the total negative zonal shear that leads to the maximum Sh^2 at NDT = π (Figure 6a). Similarly, the shear tendency term is positive during NDT = π to 2π, leading to the minimum Sh^2 at NDT = 2π. The stretching term (Figure 6d) dominates the temporal variations of the zonal shear during the N-S and S-N phases. The zonal advection term is in phase with the total tendency term, reaching its largest values between the S and S-N phases (Figure 6c). The meridional advection term (Figure 6c) is mostly negligible, except during the period between 1.5–2 π and 0–0.5 π, when its negative tendency acts to increase the total Sh^2. The vertical advection term is largest in S and S-N phases but has the opposite sign and acts to increase the total Sh^2.

The stable background stratification imposes a positive N^2 throughout the TIW cycle (Figure 7a). The time rate changes of N^2 are positive during the N-S and S phases (NDT = 0.5π to 1.2π), meaning the increase of the total background stratification (Figures 7b–7d). The combination of meridional advection, vertical advection, and differential advection of buoyancy effects yields a positive time rate of change of N^2 during NDT = 0.5 to 1.2π, leading to the maximum N^2 at NDT = 1.2π, consistent with observations (compare Figures 7a and 4c) and also shown in the southward flow phase of Figure 5. Note that this increased stratification could have stabilized the water column even under the increased Sh^2 that was partly caused by stretching, and it could have possibly led to the observed minimum in mixing during the S-N phase, which is discussed in section 5.

Similarly, the meridional and vertical advection terms (Figure 7b) enhance the stratification during the S and S-N phases, and in general, the zonal advection term is relatively small compared to the meridional advection term. The stratification tendency and differential advection of buoyancy terms are negative during the S-N to early N phases (NDT = 1.2π to 2π) and act to decrease the total background stratification (Figure 7c).

In both budgets, the tendency terms follow the sum of the right-hand side of equations. However, the residual terms are large (Figures 6e and 7d). The residual can arise from other terms not estimated in the budgets such as mixing processes, and from errors associated with, for example, the daily-averaged output and a differentiation method of the diagnostics. In the shear and stratification budgets, the residual of the former is positive and the latter is negative, indicating a tendency of reduction of Sh^2 and N^2, that may be associated with a possible effect of turbulence. If the residual term represents any mixing processes, those processes become largest around S phase. Although we cannot distinguish horizontal and vertical mixing effects, it indicates that mixing could play a role when the leading edge of the TIWs approaches the equator.

5. Discussion

5.1. Dependence of Turbulence on TIW Phases

The vertically averaged composites of Sh^2 and N^2 of the observed TIWs exhibited a clear dependence on the TIW phase, but this dependence was less clear for vertical diffusivity K_T and subsurface heat flux H_F (Figure 4). To better isolate the effect of the TIW cycle on turbulence, we applied a band-pass filter (10–40 days) on the vertically averaged Sh^2, N^2, K_T, and H_F observed by the EQUIX mooring (using data from

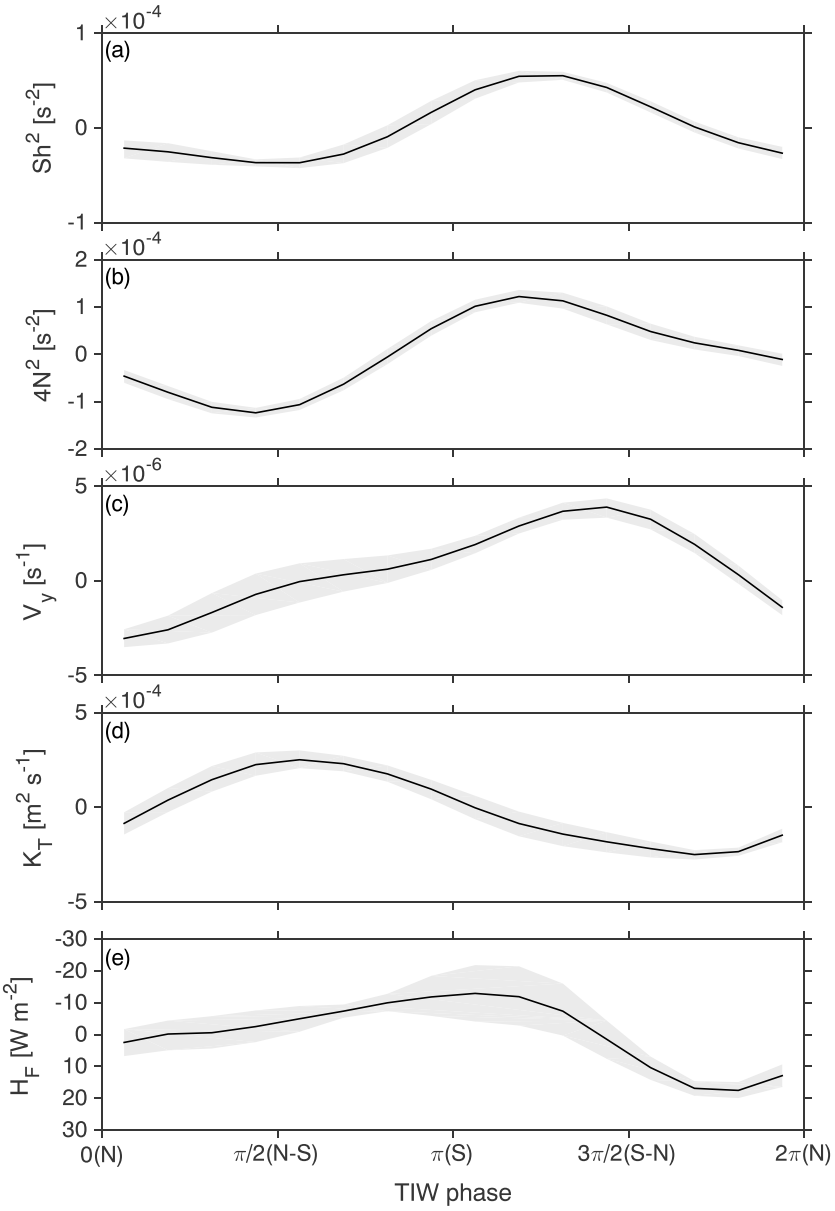

Figure 8. Plots for the composite observed tropical instability wave (TIW) showing the mean band-pass filtered vertically averaged (a) shear squared, (b) buoyancy frequency squared times 4, (c) meridional gradient of meridional velocity, (d) vertical diffusivity, and (e) heat flux. The gray shading represents 95% confidence intervals estimated by the bootstrap method (Efron & Gong, 1983). Observations from the first TIW were not used because of the data gap between the intensive and extensive observational periods, and for (c), data from the first and second TIWs were not used because of Tropical Atmosphere Ocean (TAO) buoy maintenance.

the extensive observational period) as well as $\partial_y V$ (using data from only the third through sixth TIWs due to a data gap from the TAO buoy).

Hourly average velocities with a vertical resolution of 5 m were also obtained from an ADCP on the TAO buoy, approximately 9 km south of the EQUIX mooring. By ignoring the zonal separation between the two moorings and assuming a constant separation distance of 9 km, we estimated the meridional gradient of horizontal velocities from the difference in velocities between the two mooring sites. Holmes and Thomas (2015) have suggested that the meridional gradient of meridional velocity ($\partial_y V$) are important in controlling the tendency of vertical zonal shear, $\partial_t(\partial_z U)$, at the leading edge of TIWs through the

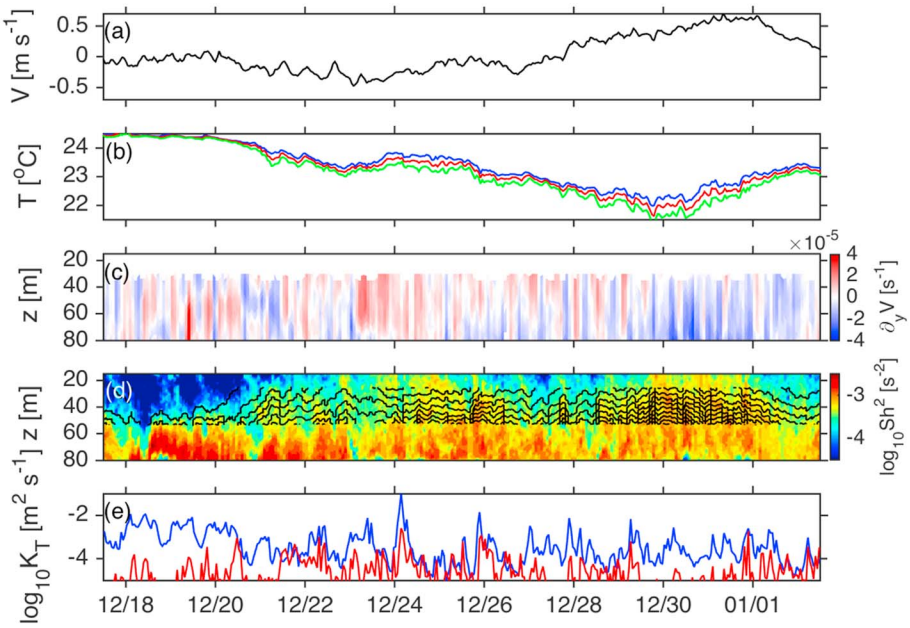

Figure 9. Time series between 18 December 2008 and 2 January 2009 showing observations of hourly (a) vertically averaged meridional velocity, (b) temperature from the first conductivity-temperature-pressure (CTD; blue line, ~25-m depth), fifth CTD (red line, ~30 m), and ninth CTD (green line, 35 m), (c) meridional gradient of meridional velocity from the Tropical Atmosphere Ocean (TAO) and Equatorial Internal Wave Experiment (EQUIX) moorings, (d) shear squared (color) and temperature (contours with 1 °C interval), and (e) K_T from averages between the first and fourth χpods (in the deep-cycle layer around 30–55 m, blue line) and from averages between the fifth and sixth χpods (above the Equatorial Undercurrent around 60–80 m, red line).

vortex stretching term, $\partial_z U \partial_y V$, which dominates over the tilting term, $-\partial_z V \partial_y U$. When $\partial_z U$ above the Equatorial Undercurrent has a large negative value, the stretching term could be large relative to the tilting term. Therefore, it is possible that a positive value of $\partial_y V$ contributes to the negative tendency of vertical shear, increases shear squared, and overcomes increasing stratification, which then leads to intense turbulence.

The band-passed K_T and H_F values in the composite observed TIWs reveal variations over the TIW cycle (Figures 8d and 8e). The K_T anomaly is positive in the N-S phase when N^2 is weakest. After the N-S phase, the band-passed $\partial_y V$ becomes positive, Sh^2 and N^2 increase, and K_T decreases because of stronger N^2, despite the strong Sh^2. Although the mean H_F is negative, the band-pass filtered H_F is positive in the S-N phase due to the weak K_T, leading to a weaker overall H_F. One strong mixing event during the S phase of the fourth TIW coincided with increasing $\partial_y V$ is described in the next section.

Finally, Holmes and Thomas (2015) predicted the large H_F variation (on the order of 100 W/m^2) within a TIW period (e.g., Figure 10 in Holmes & Thomas, 2015). Here the observed H_F variation at the EQUIX mooring is considerably smaller (~40 W/m^2; Figure 8e). We point out that Richardson number in their simulations indicated the stable state during the minimum zonal shear period, while our observation indicated the marginal stability (Figure 4) and it is a period when the deep-cycle turbulence due to diurnal surface buoyancy forcing was observed. We hypothesize that other processes such as diurnal surface buoyancy forcing (e.g., Pham et al., 2013; Smyth et al., 2013; Smyth & Moum, 2013), which were not included in their one-dimension model, could also be important for equatorial mixing.

5.2. Mixing Event in December 2008

The largest values of K_T (~7×10^{-3} m^2/s) and H_F (approximately −1,000 W/m^2) occurred during the S phase of the fourth TIW (not shown). During the N-S phase (between 18 and 20 December 2008; Figure 9a), the potential temperature was warm for all depths shown in Figure 9b, and N^2 above the Equatorial Undercurrent was weak (as evidenced by the nearly homogeneous potential temperatures at

different depths). The penetration of high Sh^2 to the base of the mixed layer and strong mixing in the deep-cycle layer were observed during nighttime (Figure 9d and blue line in Figure 9e, respectively). Between 22 and 25 December, with the weak southward flow, the potential temperature decreased and N^2 increased (as evidenced by the larger spread in temperature with depth). The potential temperature slightly increased, $\partial_y V$ became increasingly positive (Figure 9c), and the strongest mixing was observed on 24 December (Figure 9e). Given that the strong mixing during the fourth TIW likely coincided with the positive $\partial_y V$, it may be that dynamics in the leading edge of the TIW (Holmes & Thomas, 2015) contributed to the strengthened mixing observed during the S phase of this TIW. In and after the S-N phase (between 28 and 30 December), potential temperature decreased and N^2 remained high. Mixing was suppressed during this period. Then, in the N phase of the fifth TIW (beginning after 30 December), potential temperature started to increase again, N^2 and Sh^2 remained high, while $\partial_y V$ became negative. We hypothesize that this is likely due to horizontal advection of the northern edge of a front existed in the south of equator (e.g., Figure 1e). N^2 and Sh^2 started to decrease after 1 January.

6. Summary

Data from the EQUIX mooring between 23 October 2008 and 12 March 2009 captured significant variations of shear, stratification, turbulence, and turbulent heat flux in the upper central equatorial ocean during several different TIWs. This time period corresponded to the end of the 2009 La Niña, and six TIWs were fully observed by EQUIX instruments. The TIW cycle was divided into four phases on the basis of meridional velocities, and a composite TIW was generated by averaging the six observed TIWs. Results are summarized as follows:

1. Shear (Sh^2) and stratification (N^2) are weakest in the middle of the N-S phase and strongest in the late S and early S-N phases (Figures 4b and 4c). The time of peak N^2 is slightly later than the time of peak Sh^2.
2. A simulation with an OGCM demonstrated that the variations of upper ocean Sh^2 with TIW phase are primarily due to the effects of vortex stretching term in the zonal shear tendency equation, with smaller contributions from zonal and meridional shear advection (Figure 6), whereas variations of N^2 are primarily controlled by the meridional and vertical advection and differential advection of buoyancy terms in the stratification tendency equation (Figure 7).
3. The observed turbulent heat fluxes and thermal diffusivity (K_T) averaged over the deep-cycle layer were strongest during the N and N-S phases and the middle of the S phase and weakest during the S-N phase. Variations of turbulent heat flux over the TIW cycle were not as clear as the variations of K_T because vertical temperature gradient was small when K_T was large, and large when K_T was small.
4. In the N-S phase of the observed TIWs, the zone of high shear at the base of the surface mixed layer reached the depth of the high-shear zone above the Equatorial Undercurrent, leading to deep shear instability and strong turbulence. This feature is consistent with past studies (Gregg et al., 1985; Inoue et al., 2012; Moum & Caldwell, 1985; Smyth et al., 2013), and when a band-pass filter of 10–40 days was applied prior to compositing the observed TIWs, a clearer peak in thermal diffusivity emerged during the N-S phase and in turbulent heat flux during the S phase.
5. In the S phase, vortex stretching at the leading edge of TIWs (Holmes & Thomas, 2015) may have strengthened mixing because water temperature was relatively high and both Sh^2 and $\partial_y V$ increased. However, the shear instability is less favorable in the S-N phase due to strong stratification.
6. The largest values of thermal diffusivity and turbulent heat flux were observed during the S phase of the fourth TIW, which exhibited anomalous behavior (e.g., short period, distortion of the typical SST cusp pattern, and weak vertically averaged meridional velocities). The distortion of the typical TIW cycle may be due to interactions between the third and fourth TIWs or other equatorial processes (e.g., equatorial Kelvin waves). Vertical shear associated with vortex stretching is likely responsible for the intense turbulence and large flux.

In this study, we found consistent variations of stratification, shear, and turbulence during the different TIW phases within the deep-cycle layer in the EQUIX observations. The OGCM helped to identify some of the processes responsible for the variations of background shear and stratification over the TIW cycle. At the EQUIX mooring site, it is suggested that strong turbulence can be driven by the classic deep-cycle

turbulence found in 1984 (e.g., Gregg et al., 1985; Moum & Caldwell, 1985) and be modified by recently found submesoscale dynamics (e.g., Holmes et al., 2014; Holmes & Thomas, 2015). Although it was shown that the deep cycle turbulence enhances cooling in mixed layer at the equator (Moum et al., 2009, 2013), we also need to evaluate the subsurface heat flux associated with TIWs off the equator (e.g., Lien et al., 2008; Menkes et al., 2006).

Finally, previous studies have reported that in addition to turbulence, internal waves also play an important role in modifying shear and stratification (e.g., Muench & Kunze, 1999; Wijesekera & Dillon, 1991). Recent studies further pointed out the role of fronts, which generate gravity currents and internal waves (Tanaka et al., 2015; Warner et al., 2018) as well as the importance of seasonal modulation of deep cycle turbulence (Pham et al., 2017) and interaction between TIWs and equatorial Kelvin waves (Holmes & Thomas, 2016). Although this study shows dependences of turbulent mixing on the phases of the TIWs by using composite analysis, understanding how variations of background fields could alternate energy cascade processes to turbulence will be the subject of future study.

Appendix A: Description of Ocean General Circulation Model

The Modular Ocean Model (MOM4; Griffies et al., 2003) configuration used here simulates the tropical Pacific and its domain spans from 40°S to 40°N and from 120°E to 60°W. The lateral boundaries have a solid wall condition where temperature and salinity are restored to the Polar Science Center Hydrographic Climatology (Steele et al., 2001) with a damping time scale of 30 days in a 15° latitude-wide sponge region. The model is started from rest with temperature and salinity from the Polar Science Center Hydrographic Climatology. It is spun up over a 20-year period with monthly climatological surface forcing from QuikSCAT (Risien & Chelton, 2008), Massachusetts Institute of Technology–Woods Hole Oceanographic Institution objectively analyzed air-sea flux climatology (Yu et al., 2004; Yu & Weller, 2007), and long-wave and short-wave radiation climatology from the International Satellite Cloud Climatology Project (Zhang et al., 2004). After the spin-up, the model is forced with monthly QuikSCAT wind stress from September 1999 through October 2009 to cover the EQUIX period (this is an extended version of the simulation described in Perez et al., 2010).

Seven TIWs were simulated between October 2008 and early March 2009 with periods between 15 and 30 days, consistent with the mooring observations (Figures 2 and 3). Vertically averaged shear (Figures A1a and A1d) and stratification (Figures A1b and A1e) at depths of 0–60 m showed bands of positive and negative anomalies propagating westward along the equator associated with the model TIWs, with the highest values typically concentrated within ±2° latitude of the equator. Model SSTs showed TIW signatures similar to those observed by satellites (Figures A1c and A1f), with meridional velocity fluctuations (contours in Figure A1) that dominated the zonal velocity fluctuations at 0°, 140°W, similar to TAO mooring observations (Lyman et al., 2007). Although the OGCM generated TIWs with realistic spatial and temporal scales, it underestimated the meridional velocity fluctuations at 0°, 140°W. Whereas Lyman et al. (2007) observed meridional velocity fluctuations of ±80 cm/s during the 1999–2000 TIW season, the model generated meridional velocity fluctuations of ±55 cm/s during that same time period. This underestimation of the TIW kinetic energy by the model is most likely due to the model's relatively coarse horizontal resolution compared to that of more recent modeling studies (e.g., Holmes & Thomas, 2015; Marchesiello et al., 2011) as well its use of constant along-stream and cross-stream horizontal viscosities (2,000 and 1,000 m^2/s, respectively) that may be too large (Perez & Kessler, 2009). The model used the KPP parameterization (Large et al., 1994) for turbulent mixing, and we note that Holmes and Thomas (2015) pointed out the incapability of KPP parameterization for maintaining marginal stability above the Equatorial Undercurrent in their high-resolution numerical simulations. Nevertheless, the model results presented in this study provide details of the three-dimensional structure and evolution of TIWs, and they therefore elucidate mechanisms responsible for the variations of shear and stratification in the upper equatorial ocean observed at the EQUIX mooring. In the zonal shear budget, even though vertical shear by the vortex stretching was likely underestimated by our model due to the coarse resolution, the vortex stretching term usually dominates over the vortex tilting term, which is consistent with the findings of Holmes and Thomas (2015).

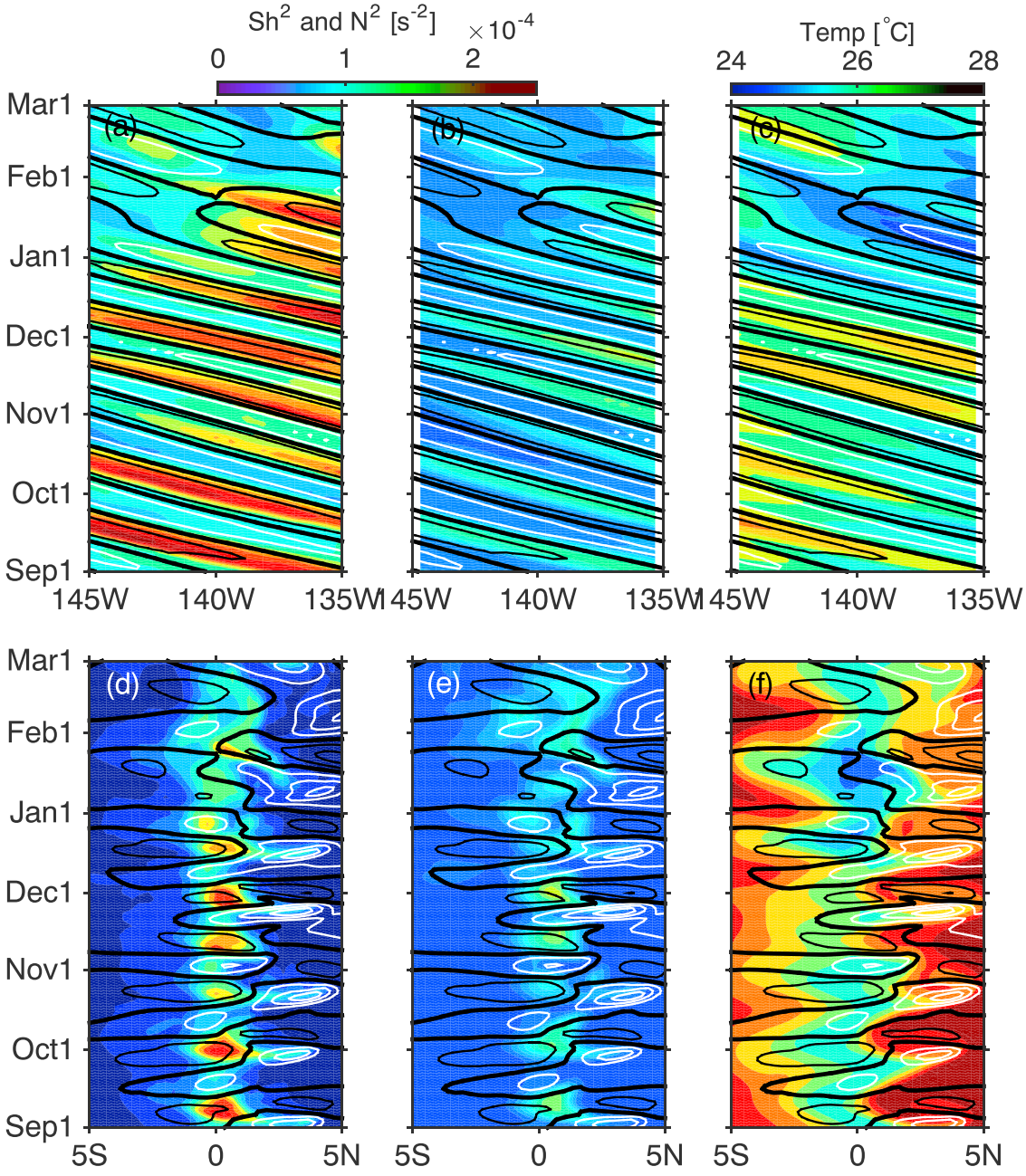

Figure A1. Progressive diagram of model simulations for the Equatorial Internal Wave Experiment (EQUIX) mooring region showing zonal (top) and meridional (bottom) profiles of (a and d) shear squared (average of 0- to 60-m depth interval), (b and e) buoyancy frequency squared (0- to 60-m average), and (c and f) temperature at 5-m depth, represented by colors. Contours represent meridional velocity (thick black line is zero, thin black lines are negative, and white lines are positive); contour interval is 0.2 m/s.

Acknowledgments

We thank Ming-Huei Chang at National Taiwan University; Jim Johnson at the University of Washington; Sasha Perlin, Ray Kreth, Daryl Swensen, and Mike Neeley-Brown at Oregon State University; and the crews of R/V *Wecoma* for the mooring operation. This work was funded by the National Science Foundation (grants 0424133, 0726523, and 0728375). We appreciate the TAO Office at NOAA's Pacific Marine Environmental Laboratory for providing surface heat flux and wind stress data (http://www.pmel.noaa.gov/tao/). The model analysis was carried out with support from the NOAA's Atlantic Oceanographic and Meteorological Laboratory. We also thank reviewers for providing many constructive comments. All data necessary to reproduce our figures are available from the corresponding author upon request (rinoue@jamstec.go.jp).

References

Baturin, N., & Niiler, P. P. (1997). Effects of instability waves in the mixed layer of the equatorial Pacific. *Journal of Geophysical Research*, *102*(C13), 27,771–27,793. https://doi.org/10.1029/97JC02455

Chereskin, T. K., Moum, J. N., Stabeno, P. J., Caldwell, D. R., Paulson, C. A., Regier, L. A., & Halpern, D. (1986). Fine-scale variability at 140-degrees-W in the equatorial Pacific. *Journal of Geophysical Research*, *91*, 2887. https://doi.org/10.1029/JC091iC11p12887

Contreras, R. F. (2002). Long-term observations of tropical instability waves. *Journal of Physical Oceanography*, *32*(9), 2715–2722. https://doi.org/10.1175/1520-0485-32.9.2715

Dutrieux, P., Menkes, C. E., Vialard, J., Flament, P., & Blanke, B. (2008). Lagrangian study of tropical instability vortices in the Atlantic. *Journal of Physical Oceanography*, *38*(2), 400–417. https://doi.org/10.1175/2007JPO3763.1

Efron, B., & Gong, G. (1983). A leisurely look at the bootstrap, the jackknife and cross-validation. *American Statistician*, *37*, 36–48.

Evans, W., Strutton, P. G., & Chavez, F. P. (2009). Impact of tropical instability waves on nutrient and chlorophyll distributions in the equatorial Pacific. *Deep Sea Research Part I: Oceanographic Research Papers*, *56*(2), 178–188. https://doi.org/10.1016/j.dsr.2008.08.008

Gregg, M. C., Peters, H., Wesson, J. C., Oakey, N. S., & Shay, T. J. (1985). Intensive measurements of turbulence and shear in the equatorial undercurrent. *Nature*, *318*(6042), 140–144. https://doi.org/10.1038/318140a0

Griffies, S. M., Harrison, M. J., Pacanowski, R. C., & Rosati, A. (2003). A technical guide to MOM4. NOAA/GFDL Ocean Group Tech. Rep. 5 (295 pp.).

Grodsky, S. A., Carton, J. A., Provost, C., Servain, J., Lorenzzetti, J. A., & McPhaden, M. J. (2005). Tropical instability waves at 0°N, 23°W in the Atlantic: A case study using Pilot Research Moored Array in the Tropical Atlantic (PIRATA) mooring data. *Journal of Geophysical Research*, *110*, C08010. https://doi.org/10.1029/2005JC002941

Halpern, D., Knox, R. A., & Luther, D. S. (1988). Observations of 20-day meridional current oscillations in the upper ocean along the Pacific equator. *Journal of Physical Oceanography*, *18*(11), 1514–1534. https://doi.org/10.1175/1520-0485(1988)018<1514:OODPMC>2.0.CO;2

Holmes, R. M., & Thomas, L. N. (2015). The modulation of equatorial turbulence by tropical instability waves in a regional ocean model. *Journal of Physical Oceanography*, *45*(4), 1155–1173. https://doi.org/10.1175/JPO-D-14-0209.1

Holmes, R. M., & Thomas, L. N. (2016). Modulation of tropical instability wave intensity by equatorial Kelvin waves. *Journal of Physical Oceanography*, *46*(9), 2623–2643. https://doi.org/10.1175/JPO-D-16-0064.1

Holmes, R. M., Thomas, L. N., Thompson, L., & Darr, D. (2014). Potential vorticity dynamics of tropical instability vortices. *Journal of Physical Oceanography*, *44*(3), 995–1011. https://doi.org/10.1175/JPO-D-13-0157.1

Hormann, V., Lumpkin, R., & Perez, R. C. (2013). A generalized method for estimating the structure of the equatorial Atlantic cold tongue: application to drifter observations. *Journal of Atmospheric and Oceanic Technology*, *30*(8), 1884–1895. https://doi.org/10.1175/JTECH-D-12-00173.1

Inoue, R., Lien, R.-C., & Moum, J. N. (2012). Modulation of equatorial turbulence by a tropical instability wave. *Journal of Geophysical Research*, *117*, C10009. https://doi.org/10.1029/2011JC007767

Jochum, M., Cronin, M. F., Kessler, W. S., & Shea, D. (2007). Observed horizontal temperature advection by tropical instability waves. *Geophysical Research Letters*, *34*, L09604. https://doi.org/10.1029/2007GL029416

Jochum, M., & Murtugudde, R. (2006). Temperature advection by tropical instability waves. *Journal of Physical Oceanography*, *36*(4), 592–605. https://doi.org/10.1175/JPO2870.1

Johnson, G. C., Sloyan, B. M., Kessler, W. S., & McTaggart, K. E. (2002). Direct measurements of upper ocean currents and water properties across the tropical Pacific during the 1990s. *Progress in Oceanography*, *52*(1), 31–61. https://doi.org/10.1016/S0079-6611(02)00021-6

Kennan, S. C., & Flament, P. J. (2000). Observations of a tropical instability vortex. *Journal of Physical Oceanography*, *30*(9), 2277–2301. https://doi.org/10.1175/1520-0485(2000)030<2277:OOATIV>2.0.CO;2

Large, W. G., McWilliams, J. C., & Doney, S. C. (1994). Oceanic vertical mixing: A review and a model with a nonlocal boundary layer parameterization. *Reviews of Geophysics*, *32*(4), 363–403. https://doi.org/10.1029/94RG01872

Lee, T., Lagerloef, G., Gierach, M. M., Kao, H.-Y., Yueh, S., & Dohan, K. (2012). Aquarius reveals salinity structure of tropical instability waves. *Geophysical Research Letters*, *39*, L12610. https://doi.org/10.1029/2012GL052232

Lien, R.-C., Caldwell, D. R., Gregg, M. C., & Moum, J. N. (1995). Turbulence variability at the equator in the central Pacific at the beginning of the 1991 93 El Niño. *Journal of Geophysical Research*, *100*(C4), 6881–6898. https://doi.org/10.1029/94JC03312

Lien, R.-C., D'Asaro, E., & McPhaden, M. (2002). Internal waves and turbulence in the upper central equatorial Pacific: Lagrangian and Eularian observations. *Journal of Physical Oceanography*, *32*(9), 2619–2639. https://doi.org/10.1175/1520-0485-32.9.2619

Lien, R. C., D'Asaro, E. A., & Menkes, C. E. (2008). Modulation of equatorial turbulence by tropical instability waves. *Geophysical Research Letters*, *35*, L24607. https://doi.org/10.1029/2008GL035860

Lyman, J. M., Chelton, D. B., deSzoeke, R. A., & Samelson, R. M. (2005). Tropical instability waves as a resonance between equatorial Rossby waves. *Journal of Physical Oceanography*, *35*(2), 232–254. https://doi.org/10.1175/JPO-2668.1

Lyman, J. M., Johnson, G. C., & Kessler, W. S. (2007). Distinct 17- and 33-day tropical instability waves in subsurface observations. *Journal of Physical Oceanography*, *37*(4), 855–872. https://doi.org/10.1175/JPO3023.1

Marchesiello, P., Capet, X., Menkes, C., & Kennan, S. (2011). Submesoscale dynamics in tropical instability waves. *Ocean Modelling*, *39*(1-2), 31–46. https://doi.org/10.1016/j.ocemod.2011.04.011

Masina, S., & Philander, S. G. H. (1999). An analysis of tropical instability waves in a numerical model of the Pacific Ocean–1. Spatial variability of the waves. *Journal of Geophysical Research*, *104*(C12), 29,613–29,635. https://doi.org/10.1029/1999JC900227

Masina, S., Philander, S. G. H., & Bush, A. (1999). An analysis of tropical instability waves in a numerical model of the Pacific Ocean. Part II: Generation and energetics. *Journal of Geophysical Research*, *104*(C12), 29,637–29,661. https://doi.org/10.1029/1999JC900226

Menkes, C. E. R., Vialard, J. G., Kennan, S. C., Boulanger, J.-P., & Madec, G. V. (2006). A modelling study of the impact of tropical instability waves on the heat budget of the eastern equatorial Pacific. *Journal of Physical Oceanography*, *36*(5), 847–865. https://doi.org/10.1175/JPO2904.1

Moum, J. N., & Caldwell, D. R. (1985). Local influences on shear flow turbulence in the equatorial ocean. *Science*, *230*(4723), 315–316. https://doi.org/10.1126/science.230.4723.315

Moum, J. N., Caldwell, D. R., & Paulson, C. A. (1989). Mixing in the equatorial surface layer and thermocline. *Journal of Geophysical Research*, *94*(C2), 2005–2022. https://doi.org/10.1029/JC094iC02p02005

Moum, J. N., Gregg, M. C., Lien, R. C., & Carr, M. E. (1995). Comparison of turbulence kinetic energy dissipation rate estimates from two ocean microstructure profilers. *Journal of Atmospheric and Oceanic Technology*, *12*(2), 346–366. https://doi.org/10.1175/1520-0426(1995)012<0346:COTKED>2.0.CO;2

Moum, J. N., Lien, R.-C., Perlin, A., Nash, J. D., Gregg, M. C., & Wiles, P. J. (2009). Sea surface cooling at the equator by subsurface mixing in tropical instability waves. *Nature Geoscience*, *2*(11), 761–765. https://doi.org/10.1038/ngeo657

Moum, J. N., & Nash, J. D. (2009). Mixing measurements on an equatorial ocean mooring. *Journal of Atmospheric and Oceanic Technology*, *26*(2), 317–336. https://doi.org/10.1175/2008JTECHO617.1

Moum, J. N., Perlin, A., Nash, J. D., & McPhaden, M. J. (2013). Seasonal sea surface cooling in the equatorial Pacific cold tongue controlled by ocean mixing. *Nature*, *500*(7460), 64–67. https://doi.org/10.1038/nature12363

Muench, J., & Kunze, E. (1999). Internal wave interactions with equatorial deep jets. Part I: Momentum-flux divergences. *Journal of Physical Oceanography*, *29*(7), 1453–1467. https://doi.org/10.1175/1520-0485(1999)029<1453:IWIWED>2.0.CO;2

Perez, R. C., Cronin, M. F., & Kessler, W. S. (2010). Tropical cells and a secondary circulation near the northern front of the equa- torial Pacific cold tongue. *Journal of Physical Oceanography*, *40*(9), 2091–2106. https://doi.org/10.1175/2010JPO4366.1

Perez, R. C., & Kessler, W. S. (2009). The three-dimensional structure of tropical cells in the central equatorial Pacific Ocean. *Journal of Physical Oceanography*, *39*(1), 27–49. https://doi.org/10.1175/2008JPO4029.1

Perez, R. C., Lumpkin, R., Johns, W. E., Foltz, G. R., & Hormann, V. (2012). Interannual variations of Atlantic tropical instability waves. *Journal of Geophysical Research*, *117*, C03011. https://doi.org/10.1029/2011JC007584

Perlin, A., & Moum, J. N. (2012). Comparison of thermal variance dissipation rates from moored and profiling instruments at the equator. *Journal of Atmospheric and Oceanic Technology*, *29*(9), 1347–1362. https://doi.org/10.1175/JTECH-D-12-00019.1

Peters, H., Gregg, M. C., & Sanford, T. B. (1991). Equatorial and off-equatorial fine-scale and large-scale shear variability at 140_W. *Journal of Geophysical Research*, *96*(C9), 16,913–16,928. https://doi.org/10.1029/91JC01317

Pham, H. T., Sarkar, S., & Winters, K. (2013). Large-eddy simulation of deep-cycle turbulence in an upper-equatorial undercurrent model. *Journal of Physical Oceanography*, *43*(11), 2490–2502. https://doi.org/10.1175/JPO-D-13-016.1

Pham, H. T., Smyth, W. D., Sarkar, S., & Moum, J. N. (2017). Seasonality of deep cycle turbulence in the eastern equatorial Pacific. *Journal of Physical Oceanography*, *47*(9), 2189–2209. https://doi.org/10.1175/JPO-D-17-0008.1

Philander, S. G. H. (1978). Instabilities of zonal equatorial currents, 2. *Journal of Geophysical Research*, *83*(C7), 3679–3682. https://doi.org/10.1029/JC083iC07p03679

Qiao, L., & Weisberg, R. H. (1998). Tropical instability wave energetics: Observations from the tropical instability wave experiment. *Journal of Physical Oceanography*, *28*(2), 345–360. https://doi.org/10.1175/1520-0485(1998)028<0345:TIWEOF>2.0.CO;2

Risien, C. M., & Chelton, D. B. (2008). A global climatology of surface wind and wind stress fields from eight years of QuikSCAT scatte- rometer data. *Journal of Physical Oceanography*, *38*(11), 2379–2413. https://doi.org/10.1175/2008JPO3881.1

Seo, H., Jochum, M., Murtugudde, R., Miller, A. J., & Roads, J. O. (2007). Feedback of tropical instability-wave-induced atmospheric variability. *Journal of Climate*, *20*(23), 5842–5855. https://doi.org/10.1175/JCLI4330.1

Smyth, W. D., & Moum, J. N. (2013). Marginal instability and deep cycle turbulence in the eastern equatorial Pacific Ocean. *Geophysical Research Letters*, *40*, 6181–6185. https://doi.org/10.1002/2013GL058403

Smyth, W. D., Moum, J. N., Li, L., & Thorpe, S. A. (2013). Diurnal shear instability, the descent of the surface shear layer, and the deep cycle of equatorial turbulence. *Journal of Physical Oceanography*, *43*(11), 2432–2455. https://doi.org/10.1175/JPO-D-13-089.1

Steele, M., Morley, R., & Ermold, W. (2001). PHC: A global ocean hydrography with a high-quality Arctic Ocean. *Journal of Climate*, *14*(9), 2079–2087. https://doi.org/10.1175/1520-0442(2001)014<2079:PAGOHW>2.0.CO;2

Tanaka, Y., Hibiya, T., & Sasaki, H. (2015). Downward lee wave radiation from tropical instability waves in the central equatorial Pacific Ocean: A possible energy pathway to turbulent mixing. *Journal of Geophysical Research: Oceans*, *120*, 7137–7149. https://doi.org/10.1002/2015JC011017

Toole, J. M., Peters, H., & Gregg, M. C. (1987). Upper ocean shear and density variability at the equator during TROPIC HEAT. *Journal of Physical Oceanography*, *17*(9), 1397–1406. https://doi.org/10.1175/1520-0485(1987)017<1397:UOSADV>2.0.CO;2

Warner, S. J., Holmes, R. M., Hawkins, E. H., Hoecker-Martínez, M. S., Savage, A. C., & Moum, J. N. (2018). Buoyant gravity currents released from tropical instability waves. *Journal of Physical Oceanography*, *48*(2), 361–382. https://doi.org/10.1175/JPO-D-17-0144.1

Wenegrat, J. O., & McPhaden, M. J. (2015). Dynamics of the surface layer diurnal cycle in the equatorial Atlantic Ocean (0°, 23°W). *Journal of Geophysical Research: Oceans*, *120*, 563–581. https://doi.org/10.1002/2014JC010504

Wijesekera, H., & Dillon, T. M. (1991). Internal waves and mixing in the upper equatorial Pacific Ocean. *Journal of Geophysical Research*, *96*(C4), 7115–7126. https://doi.org/10.1029/90JC02727

Wu, Q., & Bowman, K. P. (2007). Interannual variations of tropical instability waves observed by the Tropical Rainfall Measuring Mission. *Geophysical Research Letters*, *34*, L09701. https://doi.org/10.1029/2007GL029719

Yu, L., & Weller, R. A. (2007). Objectively analyzed air–sea heat fluxes for the global ice-free oceans (1981–2005). *Bulletin of the American Meteorological Society*, *88*(4), 527–540. https://doi.org/10.1175/BAMS-88-4-527

Yu, L., Weller, R. A., & Sun, B. (2004). Improving latent and sensible heat flux estimates for the Atlantic Ocean (1988–99) by a synthesis approach. *Journal of Climate*, *17*(2), 373–393. https://doi.org/10.1175/1520-0442(2004)017<0373:ILASHF>2.0.CO;2

Yu, Z., McCreary, J. P., & Proehl, J. A. (1995). On the meridional asymmetry and energetics of tropical instability waves. *Journal of Physical Oceanography*, *25*, 1680–1686.

Zhang, Y., Rossow, W. B., Lacis, A. A., Oinas, V., & Mishchenko, M. I. (2004). Calculation of radiative fluxes from the surface to top of atmosphere based on ISCCP and other global data sets: Refinements of the radiative transfer model and the input data. *Journal of Geophysical Research*, *109*, D19105. https://doi.org/10.1029/2003JD004457